



Cite this: *Green Chem.*, 2020, **22**, 368

Efficient reductive amination of HMF with well dispersed Pd nanoparticles immobilized in a porous MOF/polymer composite†

Vikram V. Karve,^a Daniel T. Sun,^a Olga Trukhina,^a Shuliang Yang,^a Emad Oveisi,^{a,b} Jeremy Luterbacher^a and Wendy L. Queen^{a,*a}

Aminated derivatives of 5-hydroxymethylfurfural (HMF) and furfural are critical intermediates for the pharmaceutical industry. The state-of-the-art catalysts currently used for these syntheses are mostly homogeneous in nature, motivating the design of recyclable, heterogeneous catalytic systems. As such, the present study illustrates a new method for the design of metal–organic framework (MOF)/polymer composites containing well-defined metal nanoparticles in a sustainable way. One such palladium functionalized MOF/polymer composite is then employed in the reductive amination of HMF under mild conditions. The catalyst shows excellent activity, including a high TON/TOF (h^{-1}) of 604.8/302.4 and ~94% amine yield, which is maintained over a larger number of reaction cycles (up to 15) when compared to several state-of-the-art materials, such as a commercial Pd/C (3 cycles). It is thought that the origin of the improved catalyst recyclability is due to the added polymer, poly-*para*-phenylenediamine (PpPDA), which helps to prevent the aggregation and leaching of the palladium nanoparticles. The synthetic approach is further extended to design other potential catalysts with different metallic nanoparticles (NPs).

Received 6th September 2019,
Accepted 8th November 2019

DOI: 10.1039/c9gc03140e

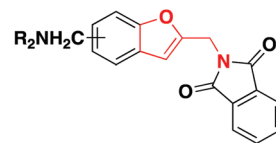
rsc.li/greenchem

Introduction

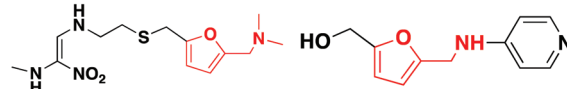
Fossil fuels are the primary source of many important chemicals; however, their impending depletion and considerable impact on climate change,¹ has spurred intense research towards replacing hydrocarbons with renewable sources.² Ligno-cellulosic biomass is one such resource that has attracted significant attention due to its high abundance.³ Further, it could be employed to produce a variety of platform chemicals, such as 5-(hydroxymethyl)-furfural (HMF) and furfural, that can potentially serve as secondary sources for the production of fine organic chemicals.⁴ This prospect has recently motivated much research devoted to studying the conversion of biomass derived HMF and furfural into a variety of value-added products.^{6–9} Interestingly, HMF and furfural are important biomass derived intermediates which can be transformed into a variety of aminated compounds that are relevant to the pharmaceutical industry. This is due to the furanmethanamine moiety in the aminated derivative, a building block

that is often found in molecules^{10–13} that are used to treat a number of disorders (Fig. 1).¹³

One of the first reports on the reductive amination of HMF describes a two-step, catalyst free conversion strategy wherein the HMF is first condensed with a primary amine under anhydrous conditions and then subsequently reduced by quantitative amounts of NaBH₄ producing 5-alkyl- and 5-arylamino-2-furyl alcohols.¹⁴ Subsequently, the selectivity and conversion of the same reaction was improved with the use of a dichlorobis(2,9-dimethyl-1,10-phenanthroline) ruthenium(II) catalyst.¹⁵ Although this catalyst performs well for the conver-



Suppression of
gastric acid
secretion in
mammals



Histamine H₂-receptor
antagonist

Anti-Hepatitis - B

^aInstitute of Chemical Sciences and Engineering (ISIC), École Polytechnique Fédérale de Lausanne (EPFL), CH-1051 Sion, Switzerland. E-mail: wendy.queen@epfl.ch

^bInterdisciplinary Center for Electron Microscopy, École Polytechnique Fédérale de Lausanne (EPFL), CH-1015 Lausanne, Switzerland

† Electronic supplementary information (ESI) available. See DOI: 10.1039/c9gc03140e

Fig. 1 Examples of biomolecules showcasing the aminoalkyl furan functionality (in red).⁵

sion, its homogeneous nature inhibits its recyclability. In this context, recyclable, heterogeneous catalysts are preferred. As such, since this time, there have been numerous reports on supported nanoparticle (NP) catalysts for the reductive amination of HMF.^{16–22} Unfortunately, a common shortfall encountered in these catalysts is their rapid loss of activity, a direct result of aggregation and leaching of the active NPs. The design of new catalysts able to resist NP aggregation and leaching will result in longer catalyst lifetimes, thereby making the catalysis more economically and environmentally viable.

Among a plethora of different materials, the choice to employ MOFs as NP supports stems from their exceptionally high internal surface areas,^{23–25} which provide easy accessibility to active sites. Further, MOFs have a tunable pore environment^{26,27} that allows the easy introduction of reactive functionalities meant to selectively facilitate a desired catalytic reaction.^{28,29} Recent research, demonstrates that the introduction of polymer guests into MOFs can improve both mechanical stability and internal surface area.^{30–32} Further, separate studies have demonstrated that porous organic polymers, having high densities of Lewis base functionality, can help to inhibit the aggregation of metallic NPs.^{33,34} Considering these aforementioned points, and the prominence of MOFs in the field of heterogeneous catalysis,³⁵ we were inspired to develop a new strategy to design MOF/polymer composites loaded with metallic NPs. For this, the MOF was first synthesized and then *in situ* polymerization was carried out using palladium nitrate as a precursor. The MOF template provides extrinsic porosity to the intrinsically non-porous polymer, poly *para*-phenylene diamine (PpPDA), which contains a high-density of amines able to coordinate Pd. Further, the selected MOFs offer accessible acidic functionality like Zr⁴⁺, Fe³⁺ or hydroxyl groups on their internal surface that can promote a dehydration reaction and hence the formation of imines that can subsequently undergo reduction to an amine by H₂ adsorbed onto the Pd NPs. We hypothesized that the short chain PpPDA polymers inserted into the MOF structure would help to inhibit NP aggregation inside the support. The resulting catalyst shows good performance in the reductive amination of HMF with a host of substrates containing primary or secondary amines (with both electron withdrawing and donating functionalities) under mild reaction conditions. We surmise that the polymer promotes the appendage of aggregation-stable palladium nanoparticles within the MOF crystallites, which we demonstrate significantly improves stability of the composite when compared to several other heterogeneous catalysts.

Results and discussion

Material design and characterization

UiO-67, [Zr₆(μ₃-O)₄(μ₃-OH)₄(BPDC)₆]^{36–40} is the point of ingress for various MOF-based catalysts owed to its high surface area, ~2500 m² g⁻¹, the presence of large tetrahedral and octahedral cages with diameters of 1.2 nm and 2.3 nm, respectively, and exceptional chemical and thermal stability.^{41–45} The stability

arises from a large number of connection points between the metal node and ligand (12-connected Zr-oxo cluster) and the strength of the coordination bond found between the carboxylate and Zr⁴⁺ ion. Given these favorable attributes, UiO-67 was first synthesized according to a previously reported procedure with slight modifications (see Experimental section). When comparing the powder X-ray diffraction (PXRD) pattern obtained from the as-synthesized material and the simulated diffraction pattern of UiO-67 (Fig. 2a), the resulting white powder is confirmed to be a highly crystalline, phase pure sample of UiO-67. Further, N₂ adsorption measurements, carried out at 77 K, reveal a type I adsorption isotherm with two steps that correspond to the two types of aforementioned cages (Fig. 2b) and a BET surface area of ~2500 m² g⁻¹.

Throughout the literature, the most common shortfall encountered in the reductive amination of HMF using heterogeneous catalysts is the aggregation and leaching of the active NPs, which results in a rapid loss of catalytic activity.^{16–22,46} In previous works, we incorporated a variety of polymers into several MOF templates.^{47–49} While that work was focused on enhancing the separation properties of a given MOF, the high density of exposed Lewis basic sites on the polymer backbone, led us to employ a similar composite for catalysis. The idea was that the Lewis basic sites might help immobilize NPs inside the MOF inhibiting aggregation/leaching during reactions. As such, we developed a new, one-step *in situ* polymerization method to simultaneously generate both the polymeric species and the Pd NPs into the as-prepared UiO-67. After the modification, the resulting composite, denoted as UiO-67/PpPDA/Pd, retains crystallinity (Fig. 2a) and a high BET surface area of ~1460 m² g⁻¹ (Fig. 2b). Pore size distribution analysis

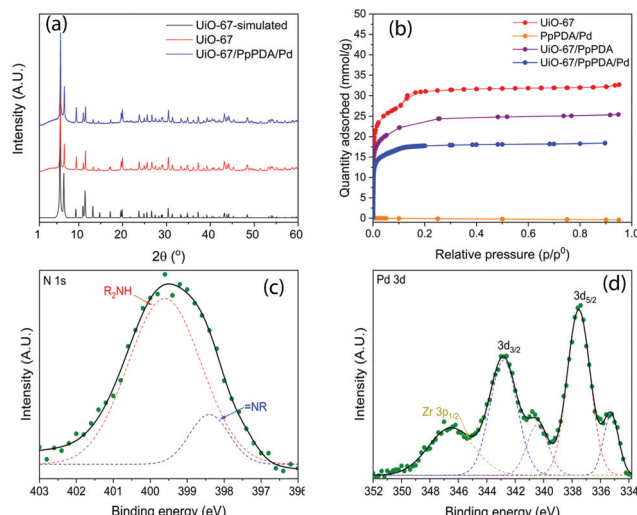


Fig. 2 Characterization of UiO-67/PpPDA/Pd. (a) X-ray diffraction patterns of the bare framework (red), the composite (blue) and the simulated pattern for UiO-67 (black). (b) N₂ adsorption isotherms at 77 K for the bare framework (red), polymer modified framework (violet), polymer and nanoparticle modified framework (blue) and the polymer-nanoparticle composite (orange). X-ray photoelectron spectroscopy analysis for the (c) N 1s and the (d) Pd 3d regions for UiO-67/PpPDA/Pd.

indicates that the polymer and Pd likely fill the largest octahedral pore (Fig. S1†). The polymer loading in the composite was determined to be 10 wt% by combustion analysis (Table T1, see ESI†), and X-ray photoelectron spectroscopy (XPS) indicates the presence of both nitrogen and Pd in the composite (Fig. 2d). The latter are present in both metallic (Pd^0) and ionized form (Pd^{2+}) in a ratio of 46% to 54%, respectively, based on the XPS spectrum. Further, the 3d peak corresponding to the Pd^{2+} species are shifted to a higher binding energy, 337.8 ± 0.6 eV (Fig. 2d), than expected, 336.7 eV, which is thought to be related to electronic interactions between the palladium and the nitrogen rich polymer.⁵⁰ We suspect that the Pd^{2+} species are coordinated to nitrogen, forming a protective shell around the metallic NPs. Further, the N 1s XPS spectrum reveals peaks that correspond to secondary and tertiary amines (Fig. 2c). These N species, which are not present in the MOF or the monomer, confirm the formation of polymeric units in the composite. MALDI-TOF-MS measurements, (Fig. S2†) carried out on the digested MOF composite, reveals oligomeric units composed of up to 8 monomers. These short chain lengths indicate that the MOF pores could play a role in limiting the polymer growth. This idea is further supported by additional polymerization experiments carried out without the MOF template, an act that expectedly results in polymers with slightly higher molecular weights with no peaks evident for low molecular weight oligomers (Fig. S3†). Attenuated total reflectance infrared (ATR-IR) spectroscopy (Fig. S4†) additionally provides qualitative evidence of polymerization. A new peak at 732 cm^{-1} corresponds to the quinoid C–N–C stretch;^{51,52} which is not expected in the monomer. Next, microscopy was used to visually inspect the resulting composite. Scanning electron microscope (SEM) images (Fig. S5†), clearly indicate that the composite has the same crystal morphology as observed for the parent UiO-67 structure. The crystallites have an average size of $\sim 200 \text{ nm}$ and relatively smooth surfaces, with no signs of polymer on the external MOF surface. In addition to this, transmission electron microscopy (BF-TEM) images show a fairly uniform distribution of Pd nanoparticles throughout the MOF (Fig. 3a). While the sizes of the NPs in the composite range from 1 to 9 nm, $\sim 60\%$ of the NPs are below 4 nm (Fig. S6†), and hence of suitable size for the inside of the defective MOF structure. It is important to note that the Zr-MOFs, such as UiO-67, often exhibit missing linkers.⁵³ These defects can lead to changes in the local pore size leading to voids that are larger than those expected from the crystal structure. Given this, titration experiments were used to investigate the existence of such linker defects (Fig. S7†). The experiments indicate that the Zr-node found in the MOF structure is indeed missing ~ 1.8 of the 6 expected linkers, a total of 30%. To confirm the presence of both the Pd nanoparticles and the polymer inside the MOF support, energy dispersive X-ray (EDX) analysis was also carried out on the composite (Fig. 3b–d, Fig. S8†). The solid powder was first embedded in a resin and sliced using a microtome. Each slice had a thickness of around 60 nm. The EDX analysis, carried out in a scanning transmission electron microscope (STEM),

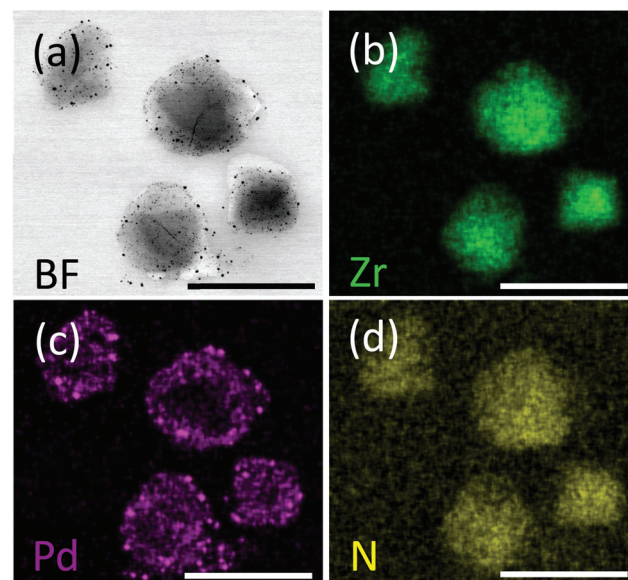


Fig. 3 BF-STEM image (a) of UiO-67/PpPDA/Pd along with the corresponding EDX maps for zirconium (b), palladium (c) and nitrogen (d) respectively. The scale bars in each image correspond to 200 nm.

reveals a uniform distribution of the nitrogen and Pd within the MOF. While this does not rule out the possibility of having a small portion of Pd NPs on the external surface of UiO-67, these experiments do indicate that there is a significant amount of the active species throughout the inside of the MOF template. For comparison, when the polymerization is carried out without the MOF present, the resulting size of the NPs inside the bulk polymer is much larger, 20 to 40 nm (Fig. S9†), supporting the idea that the MOF structure has a confinement effect on the growth of the Pd NPs.

Reaction condition optimization

To study the catalytic activity of the newly designed MOF-polymer composite, the initial aim was to optimize the reaction conditions for UiO-67/PpPDA/Pd in the reductive amination of HMF with aniline. It was expected that the reaction would proceed through the adsorption of HMF near a Lewis acidic Zr site and subsequent formation of an imine intermediate would occur upon the removal of a water molecule. Next, the imine intermediate would be reduced by the hydrogen adsorbed on the Pd NPs present in close proximity to the Zr sites throughout the framework. To evaluate this, the selected model reaction was first kept at a constant 50°C and a 5 bar H_2 pressure while the conversion of HMF and yields of the intermediate imine and final amine products were monitored as function of time (Fig. 4a). HMF conversion to the imine increases almost linearly up-to 30 minutes where the HMF conversion is completed. The imine product, which is formed through a condensation reaction between the amine group of the aniline and the aldehyde of HMF, is likely promoted by Brønsted acidic defect sites found in UiO-67.⁵³ It is noted that this intermediate is then totally converted to the

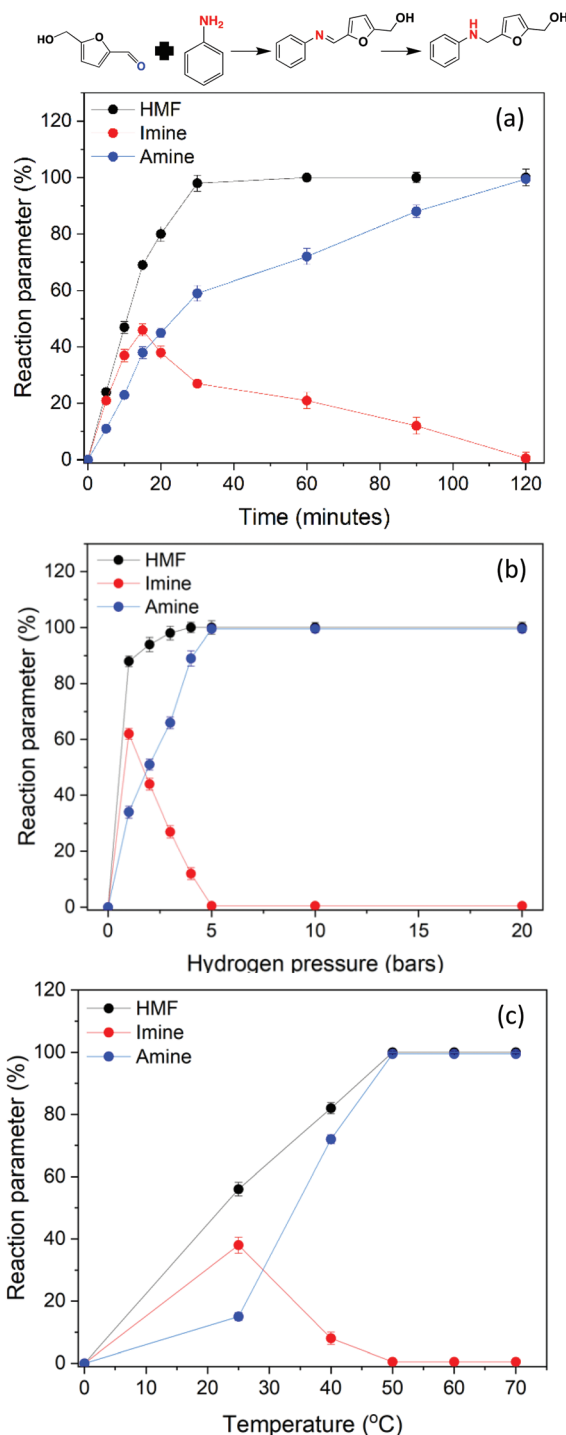


Fig. 4 Kinetic reaction profile as a function of (a) time, (b) hydrogen pressure and (c) temperature for the condensation of HMF and aniline. The black points indicate the conversion of HMF and the red and blue points indicate the yields of the imine and the amine product respectively. Reaction conditions: 10 mg UiO-67/PpPDA/Pd (0.4 wt% Pd loading), 5-hydroxymethylfurfural (0.24 mmol), aniline (0.24 mmol), 5 mL ethanol.

final amine product in 2 hours (Fig. 4a). These results indicate that the imine conversion to the amine is the rate limiting step. Next, H₂ pressure was varied (Fig. 4b), while time and

temperature were held constant at 2 hours and 50 °C, respectively. At low hydrogen pressures of 1 to 4 bar, there is incomplete conversion from the imine to the final amine product. At 5 bar, the imine shows complete conversion, and hence this pressure was selected as optimal. Finally, the conversion of HMF and the reaction products were measured as a function of temperature (Fig. 4c), with the H₂ pressure and time held at a constant 5 bar and 2 hours, respectively. Under these conditions, complete conversion into the desired amine product is indeed noted at 50 °C. Unless otherwise noted, the remainder of the reactions in this study were performed under the optimized conditions: 5 bar H₂ pressure, 2 hours, and 50 °C.

Under the selected reaction conditions UiO-67/PpPDA/Pd exhibits a high performance for the model reaction with a 94.5% yield of the targeted amine product (Table 1, entry 5). To prove that the catalysis was indeed heterogeneous in nature, a hot extraction experiment was carried out. To do this, the catalyst was removed from the reaction after 30 minutes into the process (Fig. S10†). Afterwards, no further HMF or imine conversion was observed indicating that the catalysis is indeed heterogeneous. Another indication of the composites' high catalytic activity is noted from Fig. 4c, which indicates that appreciable amounts of the imine and amine products are obtained even at room temperature. When the reaction time was extended, total conversion to the targeted amine product was observed after 10 hours at room temperature.

Evaluation of the catalytic performance under optimized conditions

Firstly, it was necessary to demonstrate that the reductive amination of HMF with aniline could not be achieved without a catalyst or in the presence of the Pd-free UiO-67 framework (Table 1, entries 1 and 2). Only UiO-67 revealed the formation of the intermediate imine, due to the MOFs ability to promote dehydration; however, the reaction showed no activity for the targeted amine, even when the reaction time was prolonged to 10 hours (Table 1, entry 3). Next, to determine if the presence of the polymer indeed can enhance catalyst performance, the catalytic activity of UiO-67/PpPDA/Pd was compared to several other Pd-containing catalysts without polymer. For this two MOFs, namely UiO-67 and Fe-BTC, were prepared and subsequently loaded with 0.40 and 0.47 wt% Pd NPs, respectively. In addition to these, a state of the art, commercially available carbon catalyst, containing 1 wt% Pd (Table 1, entries 4, 8 and 9) was purchased and tested. TEM images of UiO-67/Pd, Fe-BTC/Pd and the commercial Pd/C reveal that the Pd NPs (see methods) have sizes ranging from 4 to 9 nm (Fig. S11 and S12†), a similar size and distribution as observed for UiO-67/PpPDA/Pd. Next, PXRD was utilized to show that both UiO-67 and Fe-BTC frameworks remain crystalline after the addition of Pd (Fig. S13†).

Next, all materials were tested in the model reaction carried out under the optimized conditions. After two-hours, the two MOF/Pd samples and commercial Pd/C exhibit a high conversion efficiency and high selectivity (Table 1, entries 4, 8 and 9) as observed for UiO-67/PpPDA/Pd (Table 1, entry 5). This result

Table 1 Reaction of HMF with aniline under H_2 using various catalysts using ethanol as the solvent

Entry	Catalyst	Pd loading ^a (wt%)	Yield ^b (%)	TON/TOF ^c (h^{-1})	Cycles
1	No catalyst	—	<1%	—/—	—
2	UiO-67 ^d	—	<1%	—/—	—
3	UiO-67 ^e	—	<1%	—/—	—
4	UiO-67/Pd ^d	0.4	93%	595.2/297.6	3
5	UiO-67/PpPDA/Pd ^d	0.4	94.5%	604.8/302.4	15
6	UiO-67/PpPDA ^d	—	<1%	—/—	—
7	PpPDA/Pd ^d	0.62	<1%	—/—	Homogeneous
8	Fe-BTC/Pd	0.47	95%	608/304	1
9	Commercial Pd/C	1	82%	524.8/262.4	3

Reaction conditions: 5 bar H_2 , 50 °C, 10 mg catalyst (0.4 wt% Pd loading), 5-hydroxymethylfurfural (0.24 mmol), aniline (0.24 mmol), 5 mL ethanol. ^a Pd loading determined by ICP-OES. ^b Determined by 1H NMR. ^c Turnover number (TON) and turnover frequency (TOF) calculated for the optimized conditions for each substrate considering the total amount of Pd present in the catalyst as determined by ICP-OES. ^d Reaction time of 2 h. ^e Reaction time of 10 h.

is expected, given that all materials have accessible Pd NPs having a similar size distribution (Fig. S6, S11 and S12†). Despite similarities in the initial activity of the 4 catalysts, their differences can readily be seen with cycling. While UiO-67/Pd and Pd/C have improved longevity, they are found to be catalytically inactive after 3 cycles (Table 1, entries 4 and 9, respectively). Further analysis *via* TEM indicates an increase in NP size and a decrease in number (Fig. S12†). Unfortunately, for Fe-BTC/Pd, the catalyst is not able to tolerate the reaction conditions, and loses all activity after cycle 1 (Table 1, entry 8). TEM images taken afterwards indicate that there is a minimal amount of Pd remaining in the sample and PXRD indicates complete degradation of the MOF structure (Fig. S13†). Of the four tested catalysts, UiO-67/PpPDA/Pd, is the best performing; it has high activity in the amination reaction up to cycle 15. While TEM images taken of the sample after cycle 10 indicate minimal to no changes in the size or quantity of the Pd nanoparticles (Fig. S14†), images taken after cycle 15 indicate that most of the Pd has leached out of the sample (Fig. S15, Table T2, see ESI†).

In order to quantify Pd leaching, and hence better understand catalyst failure, UiO-67/PpPDA/Pd and the three other materials were soaked in ethanol at a temperature of 50 °C under a 5-bar pressure of H_2 for 2, 6, and 24 hours. Next, ICP-OES measurements were taken of the digested catalysts to determine the amount of Pd loss (Table T3, see ESI†). For Fe-BTC/Pd, there is a ~77% Pd loss after 2 hours, and after 6 hours, the amount of Pd remaining in the sample is below the detectable limit. Both UiO-67/Pd and Pd/C have a minimal Pd loss after 2 hours; however, after 6 hours, there is a ~65% and ~76% loss, respectively. As expected, after 24 hours, the remaining Pd is again below the detectable limit. For UiO-67/PpPDA/Pd, there is minimal Pd loss after 6 hours and only a ~15% loss after 24 hours. Further, MALDI-TOF-MS measurements taken of the ethanolic solutions indicate no apparent leaching of polymer, even after 24 hours (Fig. S16†). When considering that all MOF-based catalysts in this study have similar Pd-loadings, the aforementioned results suggest that the *N*-containing polymer plays a positive role in stabilization of the Pd NPs.

Given the significantly improved stability of the composite catalyst when compared to heterogeneous catalysts used in this study and others (Table T4, see ESI†), we carried out a more detailed investigation to assess the true stability of UiO-67/PpPDA/Pd. For this, the model reaction between HMF and aniline was again used. This time, HMF consumption and rate of amine formation was monitored for each cycle at 40% conversion (Fig. 5). In between each cycle, the catalyst was thoroughly washed and then exposed to fresh reactants. For HMF consumption, the composite catalyst shows a steady decrease in the initial rate (Fig. 6a and Fig. S17†) between cycle 1 and 15. From this, it was postulated that the decreasing HMF consumption could be due to the gradual degradation of the MOF support and/or catalyst loss upon filtration between each cycle. While we cannot rule out catalyst loss, PXRD patterns taken after every 4 cycles do indicate a gradual loss in the structural integrity of the MOF (Fig. S18†). Next, we assessed the rate of amine formation. We observe that the rate gradually increases up to cycle 3, likely related to diffusion or catalyst activation, and then appears to be steady up to cycle 10 within error of the experiment (Fig. 5b). The steady rate of amine production up to this point indicates that there is preservation of the Pd active sites, which is further supported by the aforementioned TEM images (Fig. S14†) and leaching tests carried out *via* ICP-OES (Table T3†). Unfortunately, over cycles 11 to 15, there is an incomplete conversion to the desired amine, which is accompanied by a nearly complete degradation of the MOF support (Fig. S18†). The latter lends to a noticeable leaching of the Pd active sites, as mentioned before, which is evident in TEM images taken of the composite (Fig. S15†). ICP-OES analysis reveals minimal Pd remaining in the sample after cycle 15 (Table T2†) as determined by ICP-OES analysis. It should be considered that, despite the MOF degradation, we see a nearly complete conversion of HMF at the end of the 2-hour reaction time up to cycle 10 (Fig. S19 and S20†). And, up to cycle 15, the HMF conversion decreases to only 90%. This data can be deceiving as our catalyst would look fully functional up to cycle 10, if only considering the HMF conversion and selectivity for the amine product over the reaction time. However, when looking at the HMF consumption rate, it

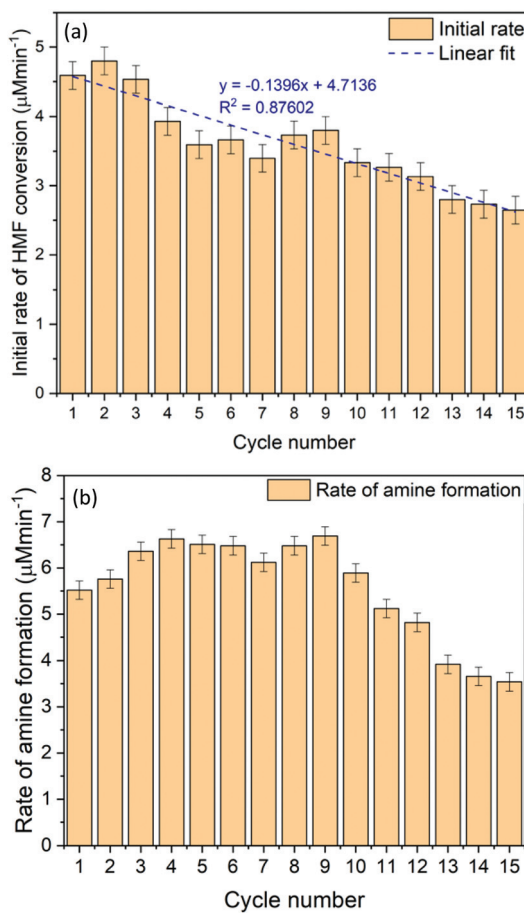


Fig. 5 Kinetic study of the recyclability probed by plotting (a) the initial rate of HMF consumption and (b) the rate of amine formation at each recycling step. Each data-point has an error bar of $0.2 \mu\text{M min}^{-1}$ calculated by triplicating the experiment; reaction conditions are HMF (0.24 mmol); amine (0.24 mmol); UiO-67/PpPDA/Pd (10 mg, 0.4 wt% Pd loading); 5 bar H_2 ; 50 °C, 5 mL ethanol, 10 minutes.

gives clearer signs of catalyst degradation (Fig. 6a) from the start. As such, we believe that kinetic studies like the one presented in Fig. 5 can be a critical indicator of true long-term catalyst cyclability.

While it is clear that UiO-67/PpPDA/Pd deactivates with repeated cycling due to MOF degradation, the rate of deactivation is significantly slowed when compared with other catalysts tested in this work and several other heterogenous catalysts reported by others (Fig. S21, Table T4, see ESI†). It is thought that the enhanced cyclability is owed to the polymer, which has high densities of Pd-complexing functionality. Further, considering that the instability is directly related to the MOF degradation, it implies that more stable supports, will lend to further extended catalyst lifetimes. It is likely that once the MOF degrades, the polymers are no longer immobilized, allowing aggregation and leaching of the Pd particles into solution. It is also noted that for the bulk polymer containing Pd nanoparticles, referred to as PpPDA/Pd, the reaction appears to be almost immediately homogeneous in nature (Table 1, entry 7). The lack of rigidity of PpPDA polymer likely permits immedi-

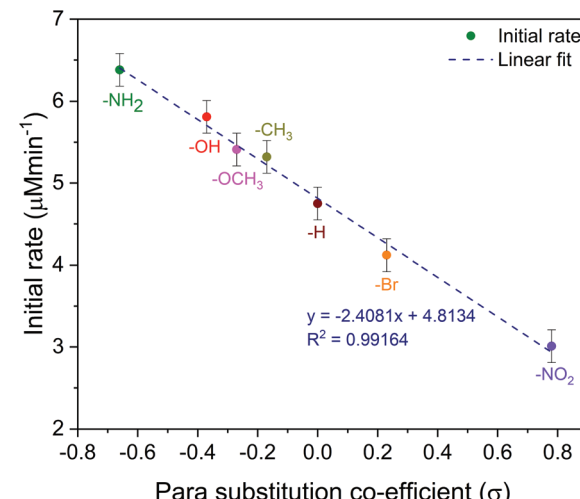


Fig. 6 Comparison of the initial rate of HMF consumption as a function of the *para* substitution Hammett co-efficient. Reaction conditions: 10 mg catalyst (0.4 wt% Pd loading), 5-hydroxymethylfurfural (0.24 mmol), aniline (0.24 mmol), 5 mL ethanol, 5 bar H_2 , 50 °C, 10 minutes.

ate aggregation of the active Pd species. The latter demonstrates the importance of the MOF in the composite.

Catalyst scope and substituent effect

After realizing the improved performance of UiO-67/PpPDA/Pd compared to the other catalysts, it was necessary to test the reductive amination of the HMF with a number of aromatic and aliphatic amines. A few secondary amines and ammonia were also tested to further expand the scope of the substrates. The data (Table 2) clearly indicates that all examined substituted anilines with both electron withdrawing and electron donating groups afford the target compounds. Secondary amines (entries 12, 15 and 16) also afforded high conversion and selectivity towards the final amino substituted product. Moreover, even when glycine is used, which has two potential condensation sites, one on the amine and a second on the hydroxyl group (entry 13, Table 2), condensation at the amino center is favoured with >99% selectivity. Clearly the data shows that UiO-67/PpPDA/Pd is a versatile catalyst for the reductive amination of HMF with a variety of substituted aromatic amines, as well as aliphatic amines, and secondary amines. To the best of our knowledge, the most efficient heterogeneous catalyst reported to date utilized 20 bar of CO at 60 °C over 2.5 h to catalyze the reductive amination using a titania supported Au catalyst. On comparison, the catalyst developed in this study has significant advantages, in terms of the turnover number (604.8), turnover frequency (302.4 h^{-1}) and cyclability as compared to the Au catalyst and other catalysts reported for reductive amination reactions. For comparison, a comprehensive list of previously reported catalysts is shown in Table S20.† To better understand the substituent effects, the reductive amination of HMF was also carried out with a series of substituted anilines having electron donating and electron

Table 2 Substrate scope using the UiO-67/PpPDA/Pd catalyst

No.	Substrate	Product	Time (h)	Yield ^a (%)	TON/TOF ^b (h ⁻¹)
1			2	94.5	604.8/302.4
2			2	91	582.4/291.2
3			2	87	556.8/278.4
4			2	68	435.2/217.6
5			2	96	614.4/307.2
6			2	93	595.2/297.6
7			2	86	550.4/275.2
8			2	80	512/256
9			2	87	556.8/278.4
10			2	90	576/288
11			2	83	531.2/265.6
12			2	91	582.4/291.2
13			2	87	556.8/278.4
14			2	87	556.8/278.4
15			2	70	448/224
16			2	92	588.8/294.4

Unless otherwise mentioned, reaction conditions are HMF (0.24 mmol); amine (0.24 mmol); UiO-67/PpPDA/Pd (10 mg, 0.4 wt% Pd); 5 bar H₂; 50 °C, 5 mL ethanol. ^a Determined by ¹H NMR. ^b Turnover number (TON) and turnover frequency (TOF) calculated for the optimized conditions for each substrate.

withdrawing substituents. For this study, each reaction was carried out over 10 minutes, which corresponds to a conversion value of 40% in case of the model reaction. The Hammett constants were used to empirically quantify and compare the effect of the substitution in the *para* position for aniline.⁵⁴ As shown in Fig. 6, there is a linear decrease in the initial rate of HMF consumption with a decrease in electronic donating character of the substituent. The effect of steric hindrance was

also probed using two substrates, including 4-toluidine and 2,4,6-trimethylaniline. The initial rate of HMF consumption was $5.1 \pm 0.2 \mu\text{M min}^{-1}$ and $4.6 \pm 0.2 \mu\text{M min}^{-1}$ for 4-toluidine and 2,4,6-trimethylaniline, respectively, indicating that the steric effect of the methyl groups in the latter compound has a mild effect on the initial rate of HMF consumption. This is likely because of the stronger cumulative electron donating effect from the larger number of methyl substituents in 2,4,6-

trimethylaniline; this can offset the stearic effect and hence help drive the reaction forward.

Design template for making novel catalysts

While porous polymers and MOFs have been used as catalysts separately, to the best of our knowledge this is the first time a MOF/polymer composite has been constructed for such an effort. The resulting composite catalyst, UiO-67/PpPDA/Pd, demonstrates a significantly improved stability when compared to the MOF (UiO-67/Pd) and polymer (PpPDA/Pd) tested separately (Table 1, entries 4 and 7). This positive attribute combined with the ease with which the catalyst building blocks can be varied, strikes our interest to design such composites for a wide array of interesting catalytic applications. For instance, one can readily vary the MOF supports (or to other porous frameworks), the stabilizing polymer additive, or the catalytically active metal NPs for a number of targeted end uses. Given this, we have also demonstrated that the active metal NPs can indeed be varied. For this, several UiO-67/PpPDA/M ($M = \text{Co, Ni and Cu}$) composite catalysts were synthesized and characterized *via* powder XRD (Fig. S22†), TEM (Fig. S23†) and N_2 sorption measurements (Fig. S24†). The testing of the utility of these catalysts for various hydrogenation reactions is currently underway and will be the basis of forthcoming reports.

Conclusions

In conclusion, a highly stable MOF/polymer composite functionalized with Pd nanoparticles, denoted as UiO-67/PpPDA/Pd, has been developed and shows excellent catalytic activity for the reductive amination of HMF. In addition to the mild reaction conditions utilized, the catalyst shows enhanced recyclability, which is superior to others reported to date. The catalyst is also highly active towards a wide variety of substrates (yields ranging from 80% to 96%) including aliphatic and aromatic amines with electron withdrawing or donating groups. The polymer inclusion into the MOF promotes a relatively homogenous distribution of small Pd NPs and significantly enhances the long-term stability of the catalyst, by a factor of 5, when compared to other non-polymer containing MOF-NP composites and a commercially available Pd/C. We surmise that this is due to the high densities of Lewis base functionality, which inhibit the aggregation of the Pd nanoparticles. Our data suggests that the eventual structural degradation of the MOF with cycling coincides with an increase in the size distribution of the Pd NPs and also an eventual loss of this active species from the composite; as such, further improving the stability of the MOF support, under the selected reaction conditions, could extend the catalyst lifetime significantly. Last, it is noted that the oxidative polymerization of *para*-phenylene diamine (or other monomers) with metal nitrates is a general method, and hence can be used as a novel platform for the design of many new heterogenous catalysts. This technique could be used to introduce aggregation stable metal NPs into

the cavities of a host of different types of porous structures aimed at a wide array of potential hydrogenation processes.

Experimental section

Materials

5-Hydroxymethylfurfural (HMF, 99%) was supplied by Fluorochem. Zirconium chloride (ZrCl_4 , 99.5%) and 1,1'-biphenyl-4,4'-dicarboxylic acid (BPDC, 98%) was obtained from ABCR. Iron(III) chloride hexahydrate (97%) was bought from Alfa Aesar and 1,3,5-benzenetricarboxylic acid (trimesic acid, 98%) was bought from ABCR GmbH. All other metal salts and chemicals were bought from Sigma Aldrich and used without further purification. Palladium nitrate ($\text{Pd}(\text{NO}_3)_2$, 99.8% metals basis) was bought from Alfa Aesar. *para*-Phenylenediamine (*p*PDA, 99.5%) was obtained from Sigma-Aldrich. Hydrochloric acid (HCl, 37%) was bought from Roth AG. Commercial Pd/C (1 wt%) catalyst was acquired from ABCR GmbH. The solvents, dimethylformamide (DMF, reagent grade), ethanol (EtOH, reagent grade) and methanol (MeOH, reagent grade) were bought from Roth AG and Reactolab SA respectively. All chemicals were used without further purification.

Characterization

Powder X-ray diffraction was performed on a Bruker D8 Discover system with a $\text{Cu K}\alpha$ source (1.54056 \AA) at 40 kV and 40 mA. The powder samples were loaded and flattened onto a zero-background silicon sample holder. The scanning range was $1\text{--}60^\circ$ over 2885 steps at a scanning rate of 2 steps per second. The simulated powder diffraction pattern of the MOFs was calculated using Mercury 3.6 crystallography software from the .CIF files of the MOFs. Nitrogen adsorption measurements were done on a Micromeritics 3flex device. Samples (50–100 mg) were activated at 150°C under vacuum for 12 hours. Nitrogen isotherms were obtained using incremental exposure of ultra-high purity nitrogen in a liquid nitrogen dewar at 77 K. The specific surface area was calculated by the BET method between a P/P_0 range of 0.03–0.3. X-ray photoelectron spectroscopy measurements were carried out using a Physical Instruments AG PHI VersaProbe II scanning XPS microprobe. Experiments were performed with a beam size of $100\text{ }\mu\text{m}$ using a monochromatic $\text{Al K}\alpha$ X-ray source of 24.8 W power. The spherical capacitor analyzer was set at 45° take-off angle with respect to the sample surface. The pass energy was 46.95 eV yielding a full width at half maximum of 0.91 eV for the $\text{Ag 3d }5/2$ peak. The data was analyzed using the CasaXPS software. Scanning Electron Microscopy (SEM) images were taken using a FEI Teneo. Samples were sputter-coated with iridium ($\sim 7\text{ nm}$ thick) in a Quorum-Q150 to minimize electron charging effects. SEM images were acquired using an in-column (Trinity) detector at an accelerating voltage of 4.0 kV. SEM-EDX data were acquired using an X-Flash silicon drift detector (Bruker) at an accelerating voltage of 10 kV. Transmission electron microscopy (TEM) images were taken

on a Tecno Spirit TEM device with an accelerating voltage of 200 kV. High-angle annular dark-field scanning transmission electron microscopy (HAADF-STEM) imaging and corresponding STEM-EDX spectroscopy were performed on a FEI Titan Themis 60–300 operated in scanning mode at an accelerating voltage of 200 kV. This microscope is equipped with a high brightness X-FEG gun and four silicon drift Super-X EDX detectors. Sample preparation for STEM measurements was done using ultramicrotomy. A resin-embedded composite was serially sectioned in ~60 nm thick slices that were deposited on a TEM grid with an ultrathin carbon support film. ATR-IR spectra were collected using a PerkinElmer Frontier MIR/FIR spectrometer equipped with a Quest ATR attachment. The sample was pressed on a diamond window and the spectra were recorded between 4000 and 400 cm^{-1} at a resolution of 4 cm^{-1} . The thermogravimetric analysis curve was obtained using a TA Q-Series TGA Q500. Samples were loaded onto a tared platinum pan. The balance flow rate was at 10 mL min^{-1} with nitrogen and the sample flow rate was at 25 mL min^{-1} with air heating at a rate of 5 °C per minute. For polymer characterization matrix-assisted laser desorption/ionization time of flight mass spectrometry (MALDI-TOF-MS) analysis was performed using a Bruker Microflex. Composites were digested in a 5 mL aqua regia solution followed by treatment in a microwave for 2 hours. A 10 mg mL^{-1} DHB (2,5-dihydroxybenzoic acid) matrix consisting of $\text{H}_2\text{O}/\text{acetonitrile/trifluoroacetic acid}$ with a 49.9/50/0.1 ratio was mixed with the solution of the digested composite, previously diluted 100 times, at a 1 to 1 ratio. 2 μL was drop casted onto a sample plate and allowed to dry in air completely. The mode was set to linear with a positive polarity and scanning range of 200–1500 m/z . Solution NMR spectra were recorded in deuterated solvents (CDCl_3) at room temperature on a BRUKER AVIII HD 400 spectrometer. The Bruker Topspin software package (version 3.2) and Mestrenova NMR software (version 11.0.1) were used to measure and analyze the data respectively.

Catalyst preparation

UiO-67. UiO-67 was prepared according to the reported synthetic procedure.³⁶ ZrCl_4 (2.41 g, 10.4 mmol) was sonicated in a mixture of 180 mL of DMF and 18 mL of HCl (37 wt%) in a 1 L cap-screw vessel for 15 min. BPDC (3.24 g, 13.4 mmol) and 360 mL of DMF were added to the mixture and the reaction mass was additionally sonicated for 15 minutes (BPDC does not dissolve completely) following by heating at 80 °C for 24 hours. After the reaction was finished, the crude was washed with DMF (4 × 40 mL) and solvent exchanged with EtOH (3 × 40 mL, overnight). The sample was dried at RT under vacuum for 6 hours, yielding 3.7 g of UiO-67 as white crystalline solid.

UiO-67/Pd. 100 mg of UiO-67 were dispersed in 40 mL of methanol by sonication for a period of 10 minutes. To this dispersion a solution of 1 mg of palladium nitrate in 0.68 mL of MilliQ water was added in a dropwise fashion. The resulting mixture was stirred at room temperature for 5.5 h. Subsequently, the powder was centrifuged and washed with

methanol repeatedly. Eventually, the UiO-67/Pd powder (0.4 wt% Pd by ICP-OES) was dried at room temperature in a vacuum oven at -30 inHg.

Fe-BTC. 9.72 g of iron(III) chloride hexahydrate, 3.36 g of trimelic acid and 120 mL of distilled water were loaded in a 180 mL Teflon autoclave. The reaction mixture was heated to 130 °C for 72 hours. After the reaction was cooled down to room temperature the orange solid was filtered under vacuum and washed with copious amounts of water and methanol. The resulting powder was loaded into a double thickness Whatman cellulose extraction thimble and underwent Soxhlet purification with methanol for 24 hours. The sample was subsequently dried under vacuum overnight.

Fe-BTC/Pd. 100 mg of Fe-BTC were dispersed in 40 mL of methanol by sonication for a period of 10 minutes. To this dispersion a solution of 1 mg of palladium nitrate in 0.68 mL of MilliQ water was added in a dropwise fashion. The resulting mixture was stirred at room temperature for 5.5 h. Subsequently, the powder was centrifuged and washed with methanol repeatedly. Eventually, the Fe-BTC/Pd powder (0.47 wt% Pd by ICP-OES) was dried at room temperature in a vacuum oven at -30 inHg.

UiO-67/PpPDA/Pd. 100 mg of activated UiO-67 were dispersed in 40 mL of methanol by sonication for a period of 10 minutes. 10 mg of *para*-phenylenediamine were dissolved in 1 mL of methanol and this solution was added to the MOF solution and stirred at room temperature for 1 hour. To this solution, 10 mg of palladium nitrate in 2 mL of MilliQ water was added and the solution was stirred for 1 day. Subsequently, the powder was filtered using a Buchner funnel and washed with ethanol (around 300 mL). After partial drying, the powder was further subjected to Soxhlet washings with ethanol to remove any unreacted reagents or free polymeric species. The powder was dried at room temperature in a vacuum oven at -30 inHg to obtain the final composite material (expected loading: 0.5 wt%; actual loading: 0.4 wt% Pd by ICP-OES).

Catalytic performance

The reductive amination of HMF was carried out in a stainless-steel Parr autoclave (0.45 L), equipped with a stainless-steel test-tube rack. HMF, the corresponding amine and the catalyst were transferred into Parr autoclave tubes in anhydrous ethanol. The tubes were purged thrice with gaseous hydrogen under stirring (500 rpm). After purging, the autoclave was pressurized with 5 bars of hydrogen and stirred at 50 °C for the 2 hours to form the products. After the reaction, the mother liquor was centrifuged, to remove the catalyst, and the ethanolic supernatant was rid of ethanol under vacuum using a rotary evaporator. The residue was re-dissolved in diethyl ether and dried using anhydrous magnesium sulphate. The ether rich organic layer was evacuated under vacuum to yield the final products. The product purity was analysed using ^1H NMR with deuterated chloroform as the solvent and TMS as the internal standard.

Conflicts of interest

There are no conflicts to declare.

Acknowledgements

This work was supported by the Swiss National Science Foundation (SNSF) under grant number PYAPP2_160581. V. V. K. thanks Canton of Valais for financial support of his PhD Project titled “Biomass Conversion in Metal-Organic Frameworks”. O. T. acknowledges funding from the European Union’s Horizon 2020 research and innovation program under the Marie Skłodowska-Curie Grant No. 665667. We acknowledge the Swiss-Norwegian Beam Line BM01 at European Synchrotron Radiation Facility (ESRF) for the provided beam time. The authors humbly thank Mounir Mensi and Mehrdad Asgari for their help with XPS and synchrotron powder X-ray diffraction, respectively.

Notes and references

- 1 J. W. Tester, E. M. Drake, M. W. Golay, M. J. Driscoll and W. A. Peters, *Sustainable Energy: Choosing Among Options*, MIT Press, Cambridge, MA, 2005.
- 2 L. Shuai, M. T. Amiri and J. S. Luterbacher, *Curr. Opin. Green Sustainable Chem.*, 2016, **2**, 59–63.
- 3 C. Li, X. Zhao, A. Wang, G. W. Huber and T. Zhang, *Chem. Rev.*, 2015, **115**, 11559–11624.
- 4 R. J. van Putten, J. C. van der Waal, E. de Jong, C. Rasrendra, H. Heeres and J. G. de Vries, *Chem. Rev.*, 2013, **113**(3), 1499–1597.
- 5 B. J. Price, J. W. Clitherow and J. Bradshaw, *U.S. Patent* 5750714A, 1995.
- 6 L. Hu, L. Lin, Z. Wu, S. Zhou and S. Liu, *Renewable Sustainable Energy Rev.*, 2017, **74**, 230–257.
- 7 I. Yu and D. Tsang, *Bioresour. Technol.*, 2017, **238**, 716–732.
- 8 J. Chheda, Y. Roman-Leshkov and J. A. Dumesic, *Green Chem.*, 2007, **9**, 342–350.
- 9 Y. Pagan-Torres, T. Wang, J. Gallo, B. Shanks and J. A. Dumesic, *ACS Catal.*, 2012, **2**, 930–934.
- 10 D. L. Crookes, *U.S. Patent* 4521431A, 1980.
- 11 B. J. Price, J. W. Clitherow and J. Bradshaw, *U.S. Patent* 4279819A, 1976.
- 12 J. Cooper and D. V. Lee, *U.S. Patent* 4347191A, 1980.
- 13 K. S. K. Murthy, G. Weeratunga, B. K. Radatus and K. P. S. Sidhu, *U.S. Patent* 5750714A, 1995.
- 14 A. Cukalovic and C. V. Stevens, *Green Chem.*, 2010, **12**, 1201–1206.
- 15 Z. Xu, P. Yan, W. Xu, S. Jia, Z. Xia, B. Chung and Z. C. Zhang, *RSC Adv.*, 2014, **4**, 59083–59087.
- 16 M. Zhu, L. Tao, Q. Zhang, J. Dong, Y.-M. Liu, H.-Y. He and Y. Cao, *Green Chem.*, 2017, **19**, 3880–3887.
- 17 T. Komanoya, T. Kinemura, Y. Kita, K. Kamta and M. Hara, *J. Am. Chem. Soc.*, 2017, **139**, 11493–11499.
- 18 S. Nishimura, K. Mizuhori and K. Ebitani, *Res. Chem. Intermed.*, 2016, **42**, 19–30.
- 19 J. J. Martinez, V. Nope, R. Eliana, H. Rojas, M. H. Brijaldo, F. Passos and G. P. Romanelli, *J. Mol. Catal. A: Chem.*, 2014, **392**, 235–240.
- 20 M. Chatterjee, T. Ishikaza and H. Kawanami, *Green Chem.*, 2016, **18**, 487–496.
- 21 G. Hahn, P. Kunnas, N. de Jonge and R. Kempe, *Nat. Catal.*, 2019, **2**, 71–77.
- 22 G. Liang, A. Wang, L. Li, G. Xu, N. Yan and T. Zhang, *Angew. Chem., Int. Ed.*, 2017, **56**, 3050–3054.
- 23 H. Furukawa, K. E. Cordova, M. O’Keeffe and O. M. Yaghi, *Science*, 2014, **341**, 123044.
- 24 D. J. Tranchemontagne, J. L. Mendoza-Cortes, M. O’Keeffe and O. M. Yaghi, *Chem. Soc. Rev.*, 2009, **38**(5), 1257–1283.
- 25 I. M. Hönicke, I. Senkovska, V. Bon, I. A. Baburin, N. Bönisch, S. Raschke, J. D. Evans and S. Kaskel, *Angew. Chem., Int. Ed.*, 2018, **57**(42), 13780–13783.
- 26 K. Koh, A. G. Wong-Foy and J. A. Matzger, *J. Am. Chem. Soc.*, 2009, **131**(12), 4184–4185.
- 27 Z. Wang and S. M. Cohen, *Chem. Soc. Rev.*, 2009, **38**, 1315–1329.
- 28 A. Dhakshinamoorthy and H. Garcia, *Chem. Soc. Rev.*, 2012, **41**, 5262–5284.
- 29 M. Meilikov, K. Yusenko, D. Esken, S. Turner, G. van Tendeloo and R. A. Fischer, *Eur. J. Inorg. Chem.*, 2010, 3701–3714.
- 30 S. Yang, L. Peng, D. T. Sun, M. Asgari, E. Oveisi, O. Trukhina, S. Bulut, A. Jamali and W. L. Queen, *Chem. Sci.*, 2019, **10**, 4542–4549.
- 31 J. G. Nguyen and S. M. Cohen, *J. Am. Chem. Soc.*, 2010, **132**(13), 4560–4561.
- 32 L. Peng, S. Yang, S. Jawahery, S. M. Moosavi, A. J. Huckaba, M. Asgari, E. Oveisi, M. K. Nazeeruddin, B. Smit and W. L. Queen, *J. Am. Chem. Soc.*, 2019, **141**(31), 12397–12405.
- 33 Y. Li, X. M. Hong, D. M. Collard and M. A. El-Sayed, *Org. Lett.*, 2000, **2**, 2385–2387.
- 34 J. Huang, T. Jiang, B. Han, H. Gao, Y. Chang, G. Zhao and W. Wu, *Chem. Commun.*, 2003, **14**, 1654–1655.
- 35 H. R. Moon, D.-W. Lim and M. P. Suh, *Chem. Soc. Rev.*, 2013, **42**, 1807–1824.
- 36 M. J. Katz, Z. J. Brown, Y. J. Colon, P. W. Siu, K. A. Scheidt, R. Q. Snurr, J. T. Hupp and O. K. Farha, *Chem. Commun.*, 2013, **49**, 9449–9451.
- 37 P. W. Siu, Z. J. Brown, O. K. Farha, J. T. Hupp and K. A. Scheidt, *Chem. Commun.*, 2013, **49**, 10920–10922.
- 38 G. L. Zhuang, J. Q. Bai, X. Zhou, Y. F. Gao, H. L. Huang, H. Q. Cui, X. Zhong, C. L. Zhong and J. G. Wang, *Eur. J. Chem.*, 2017, **1**, 172–178.
- 39 S. Lin, A. K. Ravari, J. Zhu, P. M. Usov, M. Cai, S. R. Ahrenholtz, Y. Pushkar and A. J. Morris, *ChemSusChem*, 2018, **11**, 464–471.
- 40 Y. L. Wei, Y. Li, Y. Q. Chen, Y. Dong, J. J. Dao, X. H. Yan and Y. B. Dong, *Inorg. Chem.*, 2018, **57**(8), 4379–4386.

- 41 L. Chen, H. Chen, R. Luque and Y. Li, *Chem. Sci.*, 2014, **5**, 3708–3714.
- 42 L. Chen, B. Huang, X. Qiu, X. Wang, R. Luque and Y. Li, *Chem. Sci.*, 2016, **7**, 228–233.
- 43 Y. Bu, F. Li, Y. Zhang, R. Liu, X. Luo and L. Xu, *RSC Adv.*, 2016, **6**, 40560–40566.
- 44 H. Xu, Y. Li, X. Luo, Z. Xu and J. Ge, *Chem. Commun.*, 2017, **53**, 7953–7956.
- 45 Y. H. Hu, J. C. Wang, S. Yang, Y. A. Li and Y. B. Dong, *Inorg. Chem.*, 2017, **56**(4), 8341–8347.
- 46 Z. Jin, D. Nackashi, W. Lu, C. Kittrell and J. M. Tour, *Chem. Mater.*, 2010, **22**(20), 5695–5699.
- 47 D. T. Sun, L. Peng, W. Reeder, S. M. Moosavi, D. Tiana, D. K. Britt, E. Oveisi and W. L. Queen, *ACS Cent. Sci.*, 2018, **4**(3), 349–356.
- 48 L. Peng, S. Yang, D. T. Sun, M. Asgari and W. L. Queen, *Chem. Commun.*, 2018, **54**, 10602–10605.
- 49 D. T. Sun, N. Gasilova, S. Yang, E. Oveisi and W. L. Queen, *J. Am. Chem. Soc.*, 2018, **140**, 16697–16703.
- 50 R. Arrigo, M. E. Schuster, Z. Xie, Y. Yi, G. Wowsnick, L. L. Sun, K. E. Hermann, M. Friedrich, P. Kast, M. Havecker, A. Knop-Gericke and R. Schlögl, *ACS Catal.*, 2015, **5**, 2740–2753.
- 51 S. Archana and R. J. Shanthi, *Res. J. Chem. Sci.*, 2014, **4**(2), 60–67.
- 52 S. Chavan, J. G. Vitillo, D. Gianolio, O. Zavorotynska, B. Civalleri, S. Jakobsen, M. H. Nilsen, L. Valenzano, C. Lamberti, K. P. Lillerud and S. Bordiga, *Phys. Chem. Chem. Phys.*, 2014, **14**, 1614–1626.
- 53 R. C. Klet, Y. Liu, T. C. Wang, J. T. Hupp and O. K. Farha, *J. Mater. Chem. A*, 2016, **4**, 1479–1485.
- 54 K. C. Gross and P. G. Seybold, *Int. J. Quantum Chem.*, 2000, **80**, 1107–1115.